Nano Research

Open Access

Research Article

A BiOI/TiO_2 heterogeneous interface-based fiber memristor for intelligent textile system and high-precision hand gestures recognition

Chao Jiang[1], Shenglong Huang[1], Yantao Yu[2], Zixiang Zhao[1], YiLun Cheng[1], Yusuf Abdullahi Hassan[3], Chuanghong Zhao[4,5], Dou Zhang[1], and Zizhao Ding[1] ✉

[1] Powder Metallurgy Research Institute, State Key Laboratory of Powder Metallurgy, Central South University, Changsha 410083, China
[2] College of Physics and Electronic Information & Research Center for Novel Solar-Blind Ultraviolet and Infrared Photoelectronic Detectors of Henan province, Luoyang Normal University, Luoyang 471934, China
[3] EPS Department of Mill Maintenace, Zijin AGM INC, Durban Backlands, Georgetown, Guyana
[4] College of Electronics and Information Engineering, Shenzhen University, Shenzhen 518060, China
[5] Guangdong Provincial Key Laboratory of Intelligent Information Processing, Shenzhen 518060, China

Cite this article: *Nano Research*, **2025**, *18*, 94907367. https://doi.org/10.26599/NR.2025.94907367

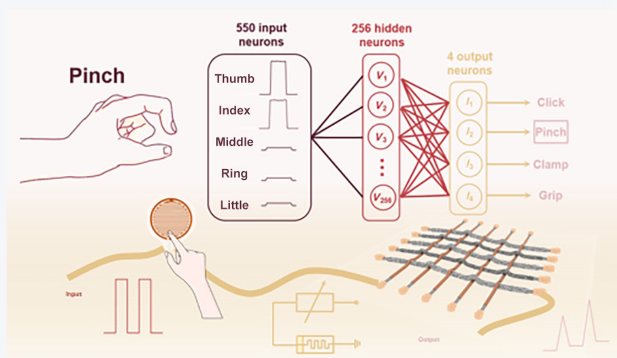

ABSTRACT: Textile memristor is the decision-making center of a bionic neuromorphic intelligent textile system and presents a promising opportunity for the incorporation of intricate information processing components within the architecture of flexible electronic textiles. This architecture, characterized by its cross-bar configuration and adaptability, positions textile memristors as a highly promising avenue for the future advancement of wearable electronic devices. Here, carbon fiber is chosen as electrode, and the memristor functional layer is made up of a high-performance and reliable BiOI/TiO_2 heterogeneous interface synthesized hydrothermally. The textile memristor exhibits an average set voltage of ≈ 0.78 V, set voltage deviation of 12.3%, long retention time (> 10^4 s), and high on/off ratio (> 10^5). Simultaneously, the observed self-rectification, room-temperature negative differential resistance (NDR) effect, and biological synaptic phenomenon offer the possibility of further neuromorphic applications. Subsequently, the pressure sensor was integrated onto the textile memristor to construct an intelligent textile system. Especially through self built datasets and neural network calculations, the gesture recognition rate of the system reached 98.5%, maintaining a high level under the influence of 20% Gaussian noise (64%). This textile memristor arrays supply great memristive performance, steady device distribution, and good mechanical strength, indicating a reliable direction for the next generation of integrated textile electrical systems.

KEYWORDS: neuromorphic computing, intelligent textile system, heterogeneous interface, textile memristor

1 Introduction

Multifunctional electronic devices with low power consumption, fast response speed, high integration, and environmental friendliness are the development trends of the next generation of electronic devices [1–3]. Nowadays, various flexible electronic components [1, 4] are recognized for their extensive potential applications within the domain of wearable electronic devices. The flexible memristor, characterized by its capabilities for multilevel storage [5, 6], high speed, and low power consumption [7], as well as its application in neuromorphic computing [8, 9], represents a significant component in the realm of wearable electronic devices.

In addition to the flexible properties of the functional layer materials, the mismatch between the functional layer materials and the substrate is a major obstacle affecting the development of the flexible memristor [1, 10]. Reducing device thickness and changing device structure and material topology are the main methods to improve the flexibility of flexible memristor [11, 12]. Because the

Received: December 30, 2024; **Revised:** March 7, 2025
Accepted: March 12, 2025

✉ Address correspondence to dingzizhao@csu.edu.cn

memristor has a crossbar structure similar to that of textiles, conductive flexible fibers can be used as both a flexible substrate and electrode to greatly simplify the flexible memristor structure [13–15]. The textile memristor with fiber substrate is considered one of the ideal directions for developing multifunctional electronics in the future.

Currently, a variety of memristor functional materials have demonstrated exemplary performance. Compared with other materials, metal oxide memristors are not sensitive to deposition conditions and can precisely control film properties [16]. As a wide bandgap n-type semiconductor, TiO_2 has the advantages of easy preparation, low cost, no toxicity, and high stability, making it a typical functional material for memristors [17]. The redistribution of charge carriers in the TiO_2 layer enables the device to effectively simulate biological synapses. However, the resistance switching may fail due to repeated formation and destruction of conductive channels [18]. Introducing other transition metal oxides into TiO_2 layer to construct a heterogeneous interface is an effective method to solve these problems, such as MnO_2/TiO_2 [17], TiO_2/CoO [19], TiO_2/HfO_2 [18], NiO/TiO_2 [20], and TiO_2/Al_2O_3 [21]. Due to the presence of local electric fields at heterogeneous interfaces, favorable transformation uniformity and low set voltage can be achieved, which has certain advantages in simulating biological synaptic functions [22]. In addition, hetero-structures show great potential in meeting self-rectifying needs to reduce sneak-path currents and circuit complexity [18, 23]. Narrow bandgap p-type semiconductor BiOI with graphene like layered structure can form a self-built internal electrostatic field [24]. Coupling with TiO_2 can significantly improve charge separation efficiency and reduce carrier charge recombination rate [24, 25]. Meanwhile, BiOI exhibits deficient energy consumption and excellent optoelectronic synaptic behavior, holding great promise for neuromorphic computing [12].

In this study, BiOI/TiO_2@carbon fibers (C_f) heterogeneous interface was synthesized via two-step hydrothermal method, while the top electrode Cu@C_f was synthesized via chemical plating, facilitating low-cost and large-scale applications. C_f were used as substrates, which can reduce the thickness of memristive devices while ensuring their mechanical strength. The textile memristor constructed using BiOI/TiO_2@C_f demonstrated several noteworthy characteristics, including a set voltage of approximately 0.78 V, an extended retention time exceeding 10^4 s, an on/off ratio greater than 10^5, set voltage deviation of less than 12.3%, and commendable mechanical properties. After treatment at 300 °C, a decrease in the set voltage (0.547 V) and its standard deviation (< 8.3%), self-rectification and room-temperature negative differential resistance (NDR) effect are observed while maintaining the same excellent memristive performance. The BiOI/TiO_2@C_f textile memristors can regulate conductivity through continuous pulses to achieve low-power biological synaptic functions, including paired pulse facilitation (PPF), and paired pulse depression (PPD). In addition, even under different pressure conditions, the device can maintain synaptic plasticity well, ensuring that the intelligent textile system can learn the electrical signals generated by external pressure stimuli. Importantly, we applied the learning methods of artificial neural networks to the recognition of hand gestures in an intelligent textile system, achieving a recognition rate of 98.5%. Under the influence of noisy datasets or pressure states, the recognition rate remains at a high level. The intelligent textile system provided here demonstrated a certain degree of neural morphology computing ability, providing a possibility for wearable intelligent electronic devices.

2 Experimental section

According to the study (Fig. 1(a)), the uniformly coated nanorods TiO_2@C_f (Fig. S1 in the Electronic Supplementary Material (ESM)) and three kinds of nano-flower BiOI/TiO_2@C_f films with different concentrations were prepared by one-step hydrothermal method and two-step hydrothermal method. With the increase of reagent concentration (0.035, 0.105, and 0.175 mmol/L), the thickness of the nano-flower BiOI film based on TiO_2@C_f increased and the flower shape became more pronounced (Figs. 1(b)–1(d) and Fig. S2 in the ESM). The sample with intermediate concentration was selected and named BiOI/TiO_2@C_f according to the morphology and subsequent performance test. The obtained BiOI/TiO_2@C_f was stored in an environment of 300 and −80 °C for a period of time to further investigate the temperature tolerance of the functional layer. The homogeneous Cu@C_f prepared by chemical plating was used as the active top electrode (Fig. 1(e)). BiOI@C_f was prepared by the same hydrothermal scheme without TiO_2 (Fig. S3 in the ESM). The synthesis of the various materials mentioned above, characterization and electrical measurements were shown in detail in the ESM.

3 Results and discussion

3.1 Structural characterizations

As shown in Figs. 1(f) and 1(g), the textile memristor comprises BiOI/TiO_2@C_f (or TiO_2@C_f, BiOI@C_f) and Cu@C_f crisscross. Figure 1(h) shows scanning electron microscope (SEM) and energy dispersive X-ray spectroscopy (EDS) images of the clear heterogeneous interface at BiOI/TiO_2@C_f cross-section. The film composed of nano-flower BiOI is uniformly coated on the TiO_2 film to form a continuous heterogeneous interface. BiOI/TiO_2@C_f was treated with ultrasound to further observe the heterogeneous interface between single nanorod TiO_2 and nano-flower BiOI. Figure 1(k) shows transmission electron microscopy (TEM) and EDS images of a single nanorod of TiO_2 and BiOI covered in a cap shape on its upper end. Low magnification TEM shows that the upper end of the nanorods TiO_2 is completely wrapped by BiOI (Fig. 1(i) and Fig. S4 in the ESM). The transmission electron micrograph of the junction of heterogeneous interface is displayed in Fig. 1(j), where d = 0.323 nm represents the crystallographic spacing of the (110) crystal layers of TiO_2. The crystallographic spacings of the (106), (201), and (004) crystal faces of BiOI in a heterogeneous interface are d = 0.143 nm, d = 0.195 nm, and d = 0.225 nm, respectively. Therefore, we can intuitively observe the formation of the heterogeneous interface between BiOI and TiO_2.

The crystal structure, purity, and type were analyzed by X-ray diffraction (XRD) (Fig. 2(a)). From all the samples, there is a broadening diffraction peak around 2θ = 21°, which should come from the offset graphene (002) crystal face caused by heat treatment destruction of graphite microcrystalline structure [26]. This phenomenon is most obvious in BiOI@C_f where the BiOI film could not completely wrap the carbon fiber. In TiO_2@C_f, clear characteristic peaks can be seen at 2θ = 27.4°, 36.1°, 41.2°, 44.0°, 54.3°, 56.6°, 62.7°, 69.0°, and 69.8° from the (110), (101), (111), (210), (211), (220), (002), (301), and (112) crystal faces of rutile TiO_2 (JCPDS No.72-1148). The diffraction peaks in BiOI@C_f can

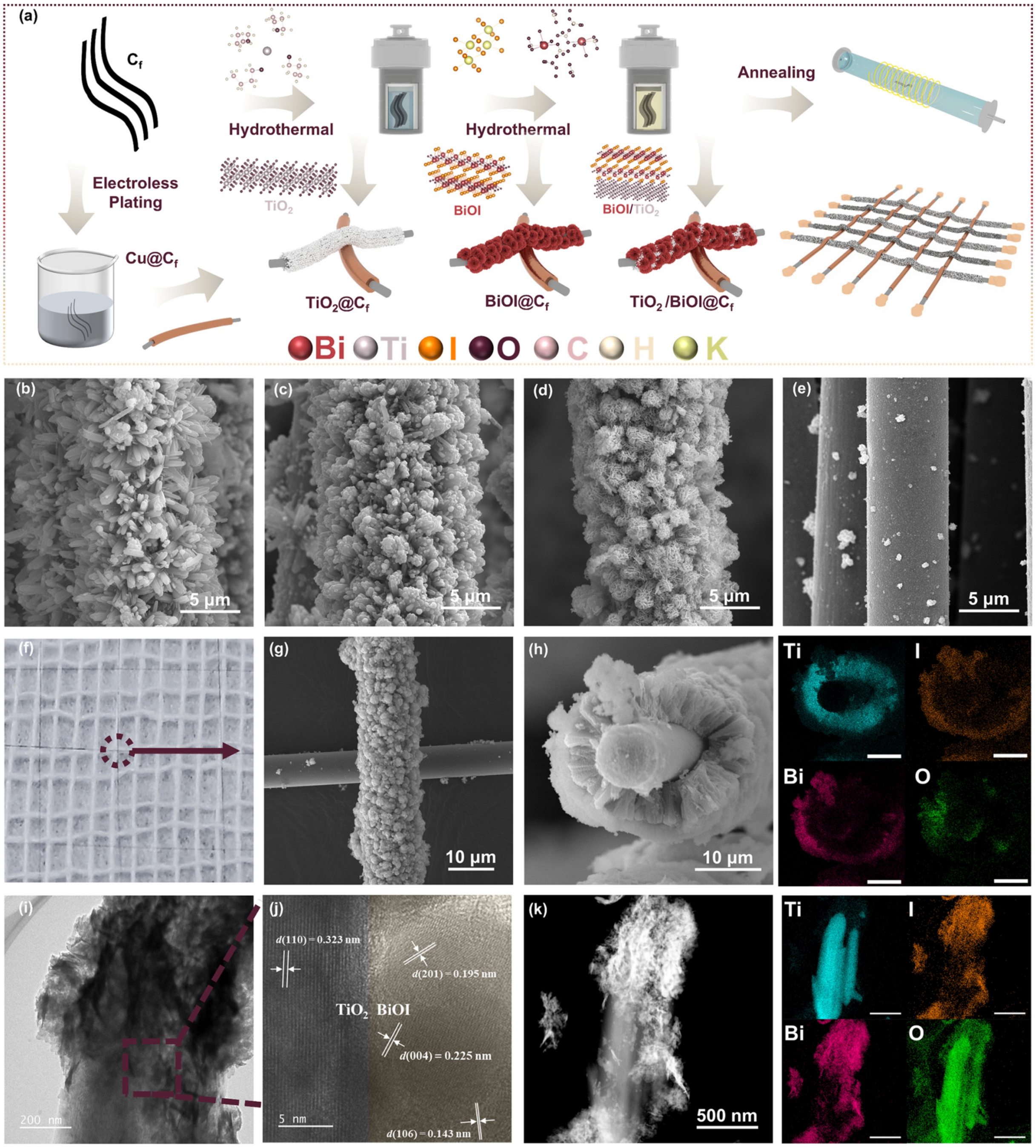

Figure 1 (a) Schematic diagram describing the formation process of textile memristors. SEM images of $BiOI/TiO_2@C_f$ with three different reagent concentrations: (b) 0.035 mmol/L, (c) 0.105 mmol/L, and (d) 0.175 mmol/L. (e) SEM image of $Cu@C_f$ prepared by chemical plating. (f) Photograph of a textile memristor consisting of 9 memristor units. (g) SEM image of a textile unit made from $BiOI/TiO_2@C_f$ and $Cu@C_f$ crisscross. (h) SEM (left) and EDS (right) images of the $BiOI/TiO_2@C_f$ cross-section. TEM images of heterogeneous interface (i) and the junction (j). (k) TEM (left) and EDS (right) images of the single $BiOI/TiO_2$.

be well index to 2θ = 9.7°, 19.4°, 24.3°, 29.7°, 31.7°, 45.4°, and 55.1° from the (001), (002), (101), (102), (110), (200), and (212) crystal faces of (JCPDS No.10-0445) tetragonal phase BiOI. The characteristic peaks of the above two single-functional layers could be observed in $BiOI/TiO_2@C_f$, indicating both materials' presence in the nanocomposites, which is consistent with the phenomena observed in the aforementioned SEM and TEM. The intensity of the characteristic peaks becomes more prominent and more diffraction peaks consistent with tetragonal phase BiOI appear after annealing in an argon atmosphere at 300 °C, which indicates that the material defects diffuse while the size of crystallites and their crystallinity increase [27].

In addition, Fig. 2(b) shows the Raman spectra of the coated carbon fiber. All observed Raman peaks can bind well with the corresponding molecular vibrational bands, and the formation of oxygen vacancies can be clearly identified through Raman spectroscopy results. Two feature peaks located at 442.1 and 607.9 cm^{-1} can be observed in $TiO_2@C_f$, corresponding to the E_g and A_{1g} vibrational mode of O–Ti–O bond, respectively. It is worth noting that an anomalously broad band at about 248.3 cm^{-1}

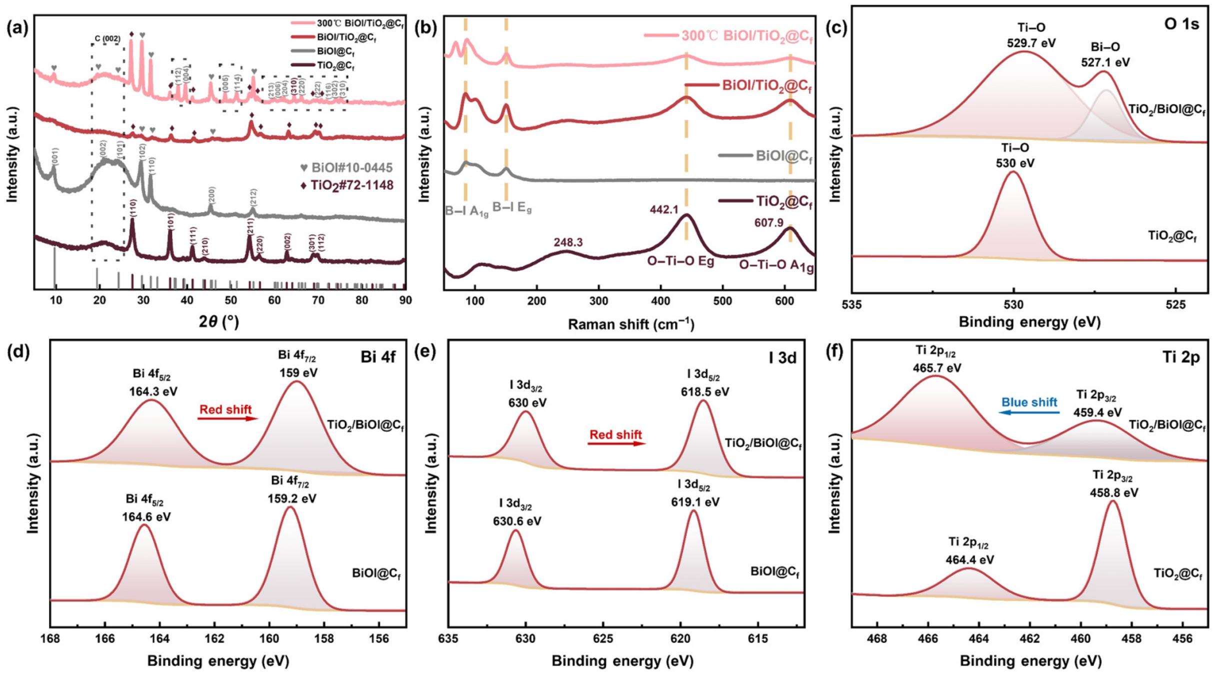

Figure 2 (a) XRD patterns, (b) Raman spectra, and XPS spectra of the $TiO_2@C_f$, $BiOI@C_f$, and $BiOI/TiO_2@C_f$: (c) O 1s, (d) Bi 4f, (e) I 3d, and (f) Ti 2p.

represents the rocking vibration of the Ti–O bond [28]. Feature peaks of 85.3 and 149.9 cm^{-1} in $BiOI@C_f$ correspond to the A_{1g} and E_g vibrational modes of Bi–I bond, respectively. Accordingly, $BiOI/TiO_2@C_f$ have feature peaks consistent with vibrational mode of O–Ti–O bond and Bi–I bond. Compared to $TiO_2@C_f$, the O–Ti–O mode region of $BiOI/TiO_2@C_f$ shows a broadening phenomenon, which may be due to the effects of oxygen vacancies and titanium unsaturated oxides brought about by the heterojunction synthesis. This feature also appears in 300 °C $BiOI/TiO_2@C_f$, demonstrating that the introduction of oxygen defects during the heat treatment process can lead to changes in the external vibrational modes of titanium-oxygen bonds and alterations in the crystal structure [29]. The presence and diffusion phenomenon of oxygen vacancies are consistent with the analysis results in XRD. The band observed at 85.3 cm^{-1} in BiOI exhibited a splitting into 68.9 and 87.2 cm^{-1} following annealing at 300 °C, suggesting a variation in the Bi–I bonding within this sample. This phenomenon may be ascribed to the presence of iodine-deficient BiOI derivatives, which are characterized by less ordered lattice structures [30].

Furthermore, X-ray photoelectron spectroscopy (XPS) analysis was utilized to investigate the surface chemical states and identify the presence of oxygen vacancies in $BiOI/TiO_2@C_f$. Meanwhile, the relative elemental content of each sample was calculated by measuring the peak area of photoelectrons (Table S1 in the ESM). Each composite material contains its respective elements Ti, O, Bi and I, according to the prepared samples' typical XPS survey spectra (Fig. S5 in the ESM). The O 1s spectra are shown in Fig. 2(c), the position of the lower peak for Bi–O species moves to a lower binding energy (from 529.7 to 527.1 eV), providing additional evidence that the connection between the two memristive functional layers is a chemical bond instead of a van der Waals interaction [29]. It is important to highlight that the red shift observed in the Bi 4f (Fig. 2(d)) and I 3d (Fig. 2(e)) peaks is associated with a blue shift in the Ti 2p (Fig. 2(f)) peaks within $BiOI/TiO_2@C_f$. These findings indicate a reduction in the electron density of Bi 4f and I 3d, while the electron density of Ti 2p rises. This phenomenon can be explained by the development of an internal electric field in $BiOI/TiO_2@C_f$, resulting from the transfer of electrons from BiOI to TiO_2. At the same time, a red shift of Ti 2p and a blue shift of O 1s were observed at 300 °C $BiOI/TiO_2@C_f$, which reflects the diffusion of oxygen vacancies in TiO_2 and the optimization of the crystal structure, consistent with the XRD and Raman results (Fig. S6 in the ESM).

3.2 The switching performance of textile memristor

The resistive switching (RS) characteristics of the textile memristor were examined through the application of a direct voltage sweep to the $Cu@C_f$ fiber electrode. For the textile memristor unit in the $TiO_2@C_f/Cu@C_f$, the observed data exhibit a characteristic nonvolatile bipolar resistive switching behavior, as evidenced by the current–voltage (I–V) curves presented in Fig. 3(a). Furthermore, there is no discernible electroforming process evident during the switching cycle. As shown in Fig. S7 in the ESM, more than sixty reproducible I–V characteristics demonstrate a high degree of uniformity in both the set and reset voltages, in addition to the switching ratio. The typical nonvolatile bipolar resistive switching behavior of the $BiOI@C_f/Cu@C_f$ is observed in Fig. 3(b) under the same conditions. The device demonstrates an increased switching ratio (> 10^4) and retention stability (> 10^3 s). However, its cyclic stability is not optimistic (Fig. S8 in the ESM). The memristive behaviors of textile memristors made of $BiOI/TiO_2@C_f$ fibers with different concentrations of BiOI added amount are compared. As the reagent concentration of BiOI increased from 0.035 to 0.105 mmol/L, the textile memristor unit showed improved switching performance and stability without the electroforming process (Fig. 3(c) and Fig. S9 in the ESM). When the concentration increases to 0.175 mmol/L, the textile memristor unit requires an ultra-high electroforming voltage, leading to a tendency to collapse in subsequent cycles (Fig. S10 in the ESM). The memristor with a reagent concentration of 0.105 mmol/L (Fig. 1(c)) was used in the following study.

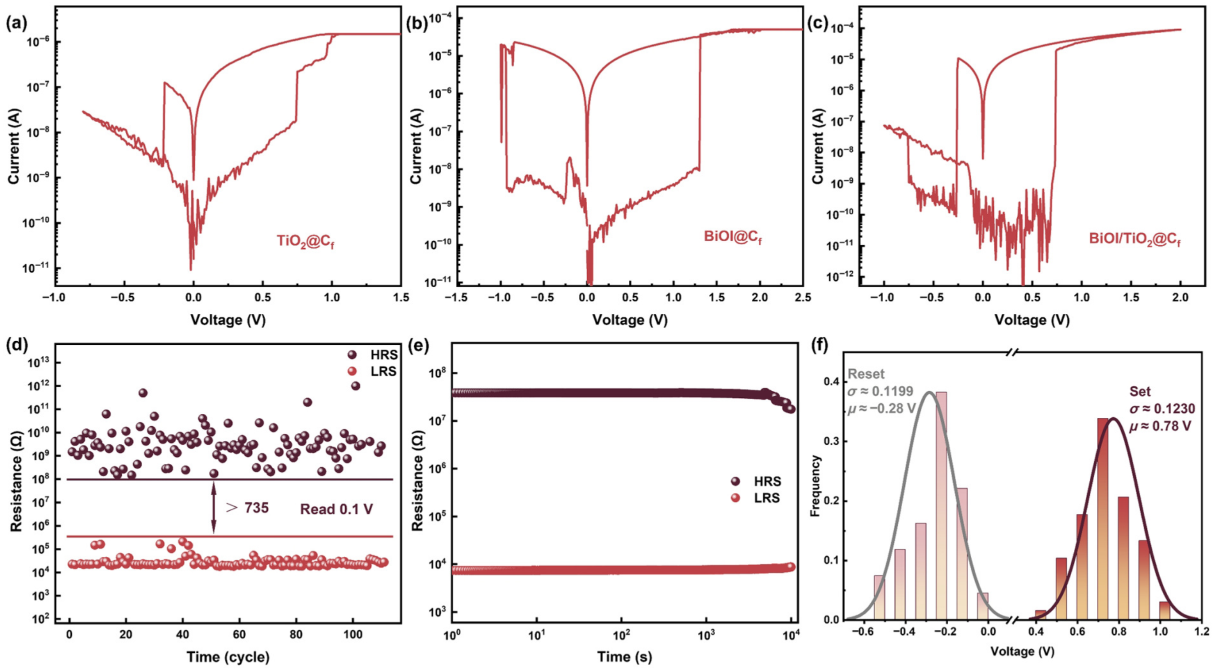

Figure 3 Typical I–V curves of textile memristor devices: (a) $TiO_2@C_f$, (b) $BiOI@C_f$, (c) $BiOI/TiO_2@C_f$, (d) endurance stability of the $BiOI/TiO_2@C_f$ device, (e) retention stability of the $BiOI/TiO_2@C_f$ device, and (f) statistical distributions of V_{set} and V_{reset}.

Afterwards, a comprehensive comparison was conducted on the memristive properties of textile memristors composed of $BiOI/TiO_2@C_f$ fibers, in relation to those of $TiO_2@C_f$ and $BiOI@C_f$. The textile memristor made of $TiO_2@C_f$ fibers exhibits an average set voltage ($V_{average}$) of 0.77 V in 60 switching cycles, with a standard deviation (V_{std}) of 0.164 V, and the variation in set voltage [14] (expressed as $V_{std}/V_{average}$, 21.4%) (Fig. S7 in the ESM). In contrast, $BiOI@C_f$ exhibits $1.48V_{average}$ in 30 cycles, with $0.691V_{std}$, and $46.8\%V_{std}/V_{average}$ (Fig. S8 in the ESM). The textile memristor constructed from $BiOI/TiO_2@C_f$ fibers demonstrates lower and more consistent set/reset voltages, exhibiting a fluctuation range of 0.49 to 1.02 V over the course of more than 100 switching cycles (Fig. S11 in the ESM). The $0.78V_{average}$, $0.123V_{std}$, and $15.8\%V_{std}/V_{average}$ are significantly better than those single-functional layer C_f (Fig. 3(f)). Both the high-resistance state (HRS) and the low-resistance state (LRS) of the $BiOI/TiO_2@C_f$ memristor units exhibit remarkable stability over 100 switching cycles, which is in stark contrast to the counterparts constructed from $TiO_2@C_f$ and $BiOI@C_f$ (Fig. 3(d) and Figs. S7(b) and S8(b) in the ESM); the average switching ratio (expressed as $R_{HRSaverage}/R_{LRSaverage} > 10^5$) and lowest switching ratio (expressed as $R_{HRSmin}/R_{LRSmax} > 734.6$) for the former are much lower than those (> 187, > 2.2; > 10^3, > 26.7) of the later. Furthermore, the memristor demonstrates a stable retention of resistance exceeding 10^4 s when subjected to a 0.1 V read voltage (Fig. 3(e)). The results show that the heterogeneous interface textile memristor combines the advantages of BiOI while maintaining the uniformity of TiO_2. In summary, the extended retention time (> 10^4 s), elevated on/off ratio (> 10^5), and consistent switching characteristics contribute significantly to mitigating crosstalk and noise challenges in crossbar array applications.

The electrical performances of textile memristor units treated at different temperatures were tested and maintained a fair degree. Figure 4(a) presents the characteristic I–V curves of a bipolar memristor composed of 300 °C $BiOI/TiO_2@C_f$. The device demonstrates consistent and reliable set/reset voltages, exhibiting a variation ranging from 0.33 to 0.91 V throughout the examination of more than 100 switching cycles. The $R_{HRSaverage}/R_{LRSaverage}$ (> 705) and R_{HRSmin}/R_{LRSmax} (> 60) are still higher than those of the $TiO_2@C_f$ and $BiOI@C_f$ (Fig. 4(b) and Fig. S7(b) in the ESM). Similarly, the memristor shows stable resistance retention of over 10^4 s under the 0.1 V read voltage (Fig. 4(c)). Notably, the I–V characteristics demonstrate a self-rectifying behavior in textile memristor units, akin to that observed in diodes. The forward-to-reverse current ratio (F/R ratio) in the LRS of the textile memristor unit serves as a quantitative measure of the rectification effect exhibited by the device [23]. This ratio is calculated based on 100 cyclic I–V curves, yielding an average value of 159, which demonstrates a significant order of magnitude difference (Fig. S12 in the ESM). In a 10 × 10 textile memristor crossbar array, the above self-rectification performance can lead to a 1.03% increase in the overall resistance of all sneak paths (Fig. S13 in the ESM) [31]. This observation illustrates the effective self-rectification behavior of $BiOI/TiO_2@C_f$, which may be attributed to the significant migration of ions in the reverse voltage direction at the heterogeneous interface. This phenomenon is crucial for minimizing the sneak current pathways, thereby facilitating the development of high-density synaptic memristor crossbar arrays and the construction of neural networks [9, 32]. It is worth noting that the significant NDR effect, characterized by a reduction in current with an increase in voltage, shows outstanding repeatability. This NDR phenomenon could result from diffusion occurring at the heterogeneous interface formed during annealing [33]. Compliance current (CC) affects the memristive behaviors of textile memristors, such as volatile versus non-volatile transitions, set and reset voltages, and device stability, possibly due to its restriction of conductive filaments (CFs) formation [12, 13]. As shown in Fig. 4(d), CC from 10^{-7} to 10^{-3} A is loaded onto the memristor and exhibits the same bipolar nonvolatile I–V curves. The textile memristor units show noticeable RS from 10^{-5} A, and the reset voltages increase significantly (from −0.1 to −2.9 V) when CC reaches 10^{-3} A. Meanwhile, the NDR

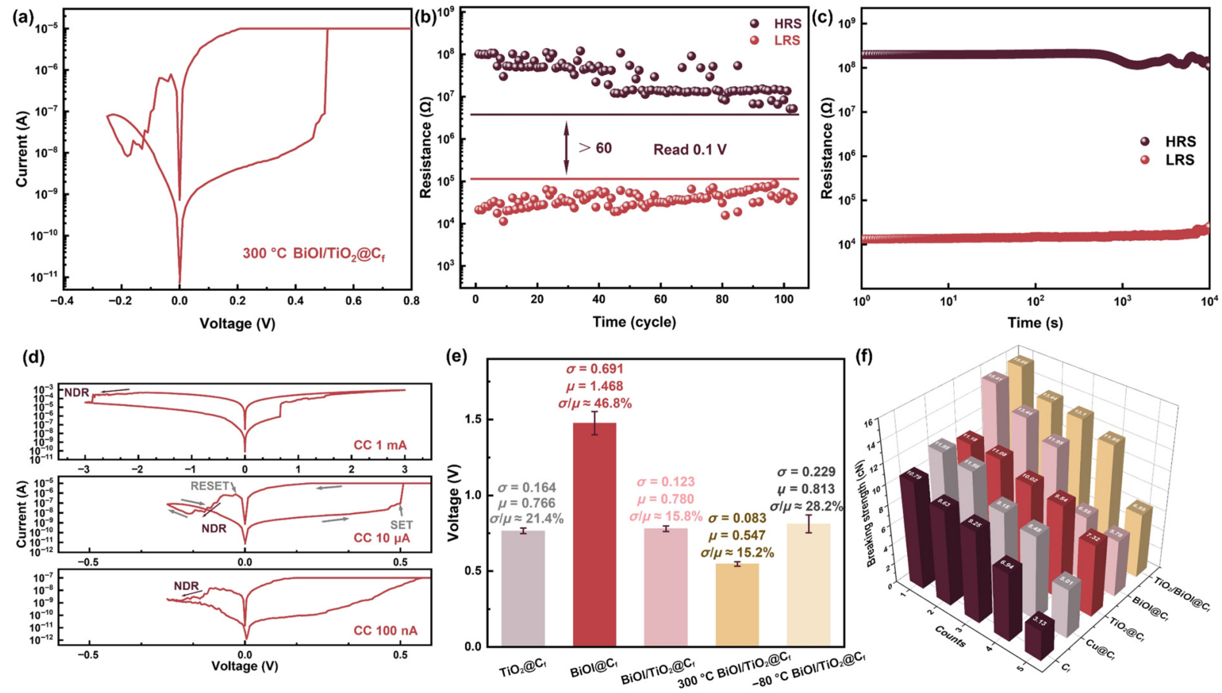

Figure 4 (a) Typical *I*–*V* curves of textile memristor device 300 °C BiOI/TiO_2@C_f. (b) Endurance stability of the BiOI/TiO_2@C_f device. (c) Retention stability of the BiOI/TiO_2@C_f device. (d) *I*–*V* curves of CC from 10^{-7} to 10^{-3} A. (e) Statistical distributions of V_{set} of five kinds selected memristor units. (f) Strength value of the prepared single textile memristor fiber.

effect gradually disappears with the increase of CC. Due to the impact of NDR on the periodic and nonlinear resistance switching of memristors, it has made significant contributions to the construction of relaxation oscillators [34] and chaotic circuits [35] for applications in sensors [36], clock circuits, and encrypted communications [37]. Consequently, the application of such BiOI/TiO_2@C_f textile memristor in the development of array-integrated neural networks could enhance circuit simplification and leverage the potential of multifunctional applications [23]. In addition, the memristor unit has a very fast response speed and long-term performance retention. Tests have shown that its response speed is less than 170 ns (Fig. S14 in the ESM), and it still maintains good performance after two months (Fig. S15 in the ESM).

The identical test was applied to −80 °C BiOI/TiO_2@C_f, revealing certain performance indicators (Fig. S16 in the ESM). The results show that the heterogeneous interface textile memristor's stability is maintained at a wide range of ambient conditions. Figure 4(e) shows the statistical data of set voltage of five kinds of selected memristor units and calculates the average value of μ, standard deviation σ, and relative fluctuation. The fabrication of heterogeneous interfaces minimizes the variability of the set voltage in memristor units, thereby enhancing their switching ratio and endurance without altering the set voltage itself. According to the representation mentioned earlier, this phenomenon can be attributed to space charge region and the local energy levels caused by significant presence of defects at the heterogeneous interface, which generate an internal electric field [17, 29]. Consequently, as heat treatment at 300 °C facilitates the diffusion of oxygen vacancies, optimizes the crystal structure, and diminishes the internal electric field, the memristor unit attains a more stable and reduced SET voltage, albeit with a slight decrease in its switching ratio. Compared with the vast majority of available planar textile memristors, BiOI/TiO_2@C_f has relatively excellent switching ratio and long-term holding time, and has the lowest set voltage among metal oxide textile memristors (Fig. S17 and Table S2 in the ESM).

In addition, through fiber strength testing and Weibull distribution analysis, the mechanical strength and dispersibility of coated carbon fiber have been significantly improved (Fig. 4(f) and Fig. S18 in the ESM). Coating the surface of carbon fibers can enhance their tensile strength, transforming brittle fracture into ductile fracture. A significant variation in strength suggests a lack of uniformity in material quality and a decrease in material reliability [38]. A Weibull analysis was performed on the tensile strength of carbon fibers to evaluate the effect of modification technology on their tensile properties. Figure S18(a) in the ESM shows a linear representation of the Weibull distribution pertaining to the tensile strength of single carbon fibers subjected to various modification processes. The Weibull modulus for the tensile fracture strength of the unmodified single carbon fiber was recorded at 4.54, which subsequently increased to a maximum of 9.56 following modification. This enhancement in the Weibull modulus signifies an improvement in the dispersibility of the tensile fracture strength of the modified carbon fiber.

3.3 Research on the mechanism of textile memristors

The diffusion of Cu atoms or ions at heterogeneous interface is a thermodynamically unfavorable process that can only occur at high temperatures or under the influence of an external electric field [39]. It can be significantly facilitated by oxygen vacancies, grain boundaries, or through the amorphous phase of oxides, promoting the formation of CFs. To further study the RS mechanism of the textile memristor, Figs. 5(a)–5(c) and Fig. S19 in the ESM show the *I*–*V* double logarithmic coordinates and the slope of the linear fit of textile memristor units under the forward bias region. Here, charge trapping and metal CFs are responsible for the RS behavior of this device.

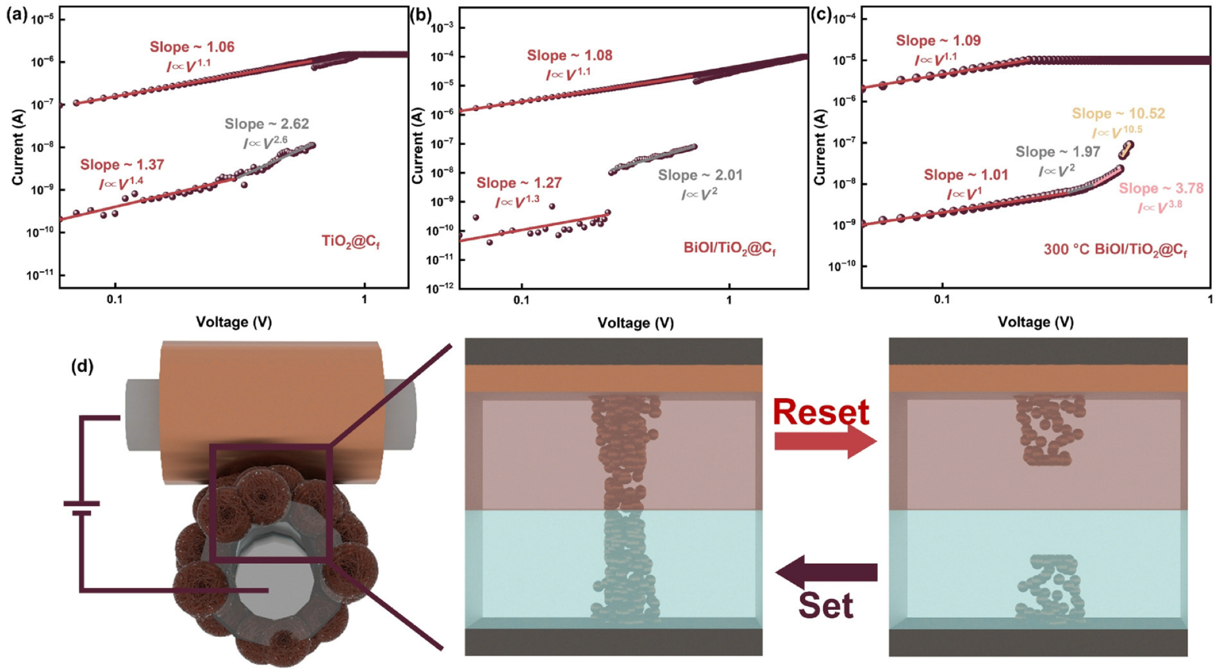

Figure 5 The forward bias region of I–V curves in double logarithmic coordinates: (a) $TiO_2@C_f$, (b) $BiOI/TiO_2@C_f$, and (c) 300 °C $BiOI/TiO_2@C_f$. (d) The schematic of the RS physical mechanism.

In the LRS, the determined fitting slopes are 1.06, 1.08, and 1.09, which suggest the presence of an ohmic conduction mechanism. The linear fitting of the I–V curve for the HRS of $TiO_2@C_f$ shows a slope of about 1.37 and 2.62 in turn, which aligns with the space charge-limited current (SCLC) mechanism controlled by the charge trapping effect of the functional layer (Fig. 5(a)). When the applied voltage is low, the injected electrons are trapped by defects in the functional layer or confined by the space charge in the heterogeneous interface barrier region [40], leaving no mobile free electrons in the film, resulting in HRS. As the applied voltage increases, electrons confined by space charge are released after continuous accumulation, and the freely moving carriers transform the device into LRS. The slopes correspond to the three stages of SCLC: Ohm's conduction law ($I \propto V$), Child's conduction law ($I \propto V^2$), and current surge stage ($I \propto V^n$, $n > 2$) [41]. The similar slopes are observed in three subsequent samples. It is worth noting that the change in the ohmic resistance state of $BiOI/TiO_2@C_f$ in the HRS is significant, making it difficult to conduct electricity (Fig. 3(c)). This may be due to the large number of oxygen vacancies capturing electrons and the strong internal electric field [42]. The depletion region is formed at the $BiOI/TiO_2$ heterogeneous interface due to the diffusion of electrons and holes. The voltage from TiO_2 to BiOI increases the width of the built-in electric field and the depletion region, where the diffusion and drift currents are in an unbalanced state, while the net current remains stable [43]. This keeps the memristor resistance stable and continuous until the voltage exceeds the heterogeneous interface tolerance limit. Moreover, the RS process becomes more stable and coherent with increasing on/off ratios after annealing, leading to a shortened charge trapping process (Figs. 5(b) and 5(c)). This may be caused by the reduction of defects caused by heat treatment and the diffusion at the heterogeneous interface.

Considering the configuration of the Cu top electrode and the C_f bottom electrode in textile memristor units, it is plausible that Cu CFs are generated within the LRS. This observation aligns with the characteristic electrochemical metallization (ECM) RS behavior, which involves the development of metallic conductive channels [12]. HRS reflects the intrinsic conduction characteristics of the memristor functional film layer. The distinct conduction mechanism of HRS and LRS indicates that the conduction mechanism of LRS is a local CFs mechanism [44]. It is reported that CFs formation depends on the competition of different nucleation positions, and the disconnection process only targets CFs that have already formed [45]. Consequently, CFs formation exhibits a greater degree of randomness compared to disconnection, which is consistent with the above V_{set} and V_{reset} statistical results, supporting the presence of CFs mechanism [46]. Therefore, the RS mechanism can be succinctly illustrated, as depicted in Fig. 5(d). When a forward voltage is applied to the textile memristor, oxidized Cu^{2+} ions are generated at the Cu electrode and move towards the C_f, where Cu^{2+} ions are reduced to Cu atoms and accumulate to form Cu CFs, resulting in LRS. Conversely, applying a reverse voltage causes the oxidized Cu^{2+} ions to return to the Cu electrode, resulting in the breaking of the established conductive channels. Charge is trapped and released during the breaking and formation of the CFs.

3.4 Intelligent textile system based on $BiOI/TiO_2@C_f$ memristor and high-precision hand gestures recognition

As shown in Figs. 6(a) and 6(b), the textile memristor is the decision-making center of a bionic neuromorphic intelligent textile system. When a pressure sensor is integrated with the textile memristor, the pressure stimulus will trigger the sensor's response, resulting in a voltage change in the memristor that produces post-synaptic current. The memory of the pressure information is represented by the change in conductivity of the memristor [47]. Combining intelligent textile systems with neuromorphic computing networks to compare and classify the EPSC datasets generated by external stimuli is of great significance for recognizing human touch, vision, and posture. As shown in Fig. 6(b)(II), a

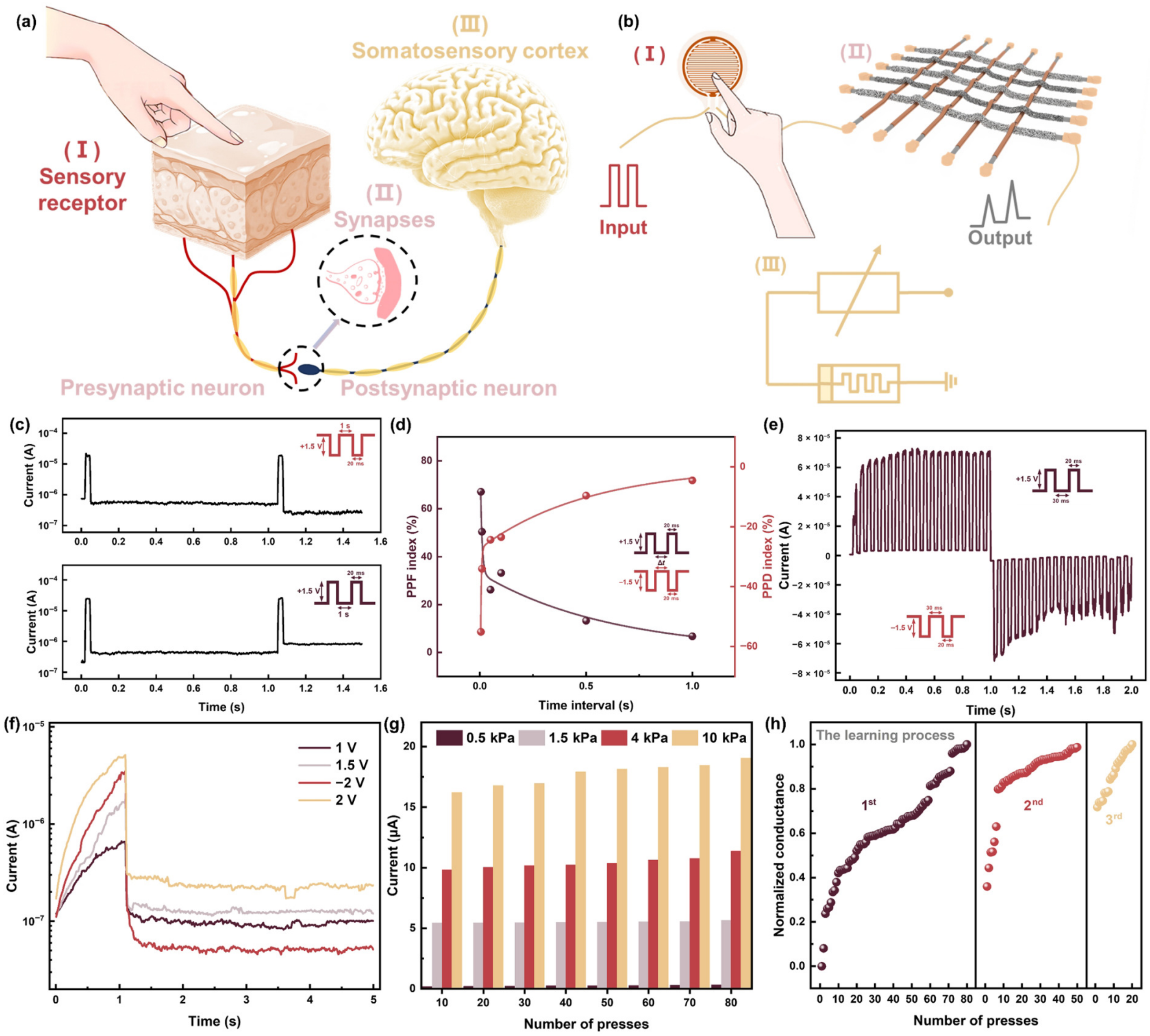

Figure 6 (a) The biological perception system consists of (I) sensory receptor, (II) synapses, and (III) the brain. (b) The intelligent textile system contains (I) a pressure sensor, (II) a BiOI/TiO$_2$@C$_f$ textile memristor, and (III) a connection circuit diagram. (c) PPF and PPD (±1.5 V amplitude, 0.02 s width, and 1 s interval). (d) Pulse interval dependent PPF and PPD index (±1.5 V amplitude, 0.02 s width, 0.005–1 s interval, brown: positive pulse, red: negative pulse). (e) Current response under positive (up) and negative (down) square-wave voltage pulses. (f) Multilevel storage caused by voltage pulses of different amplitudes. (g) The intelligent textile system can respond to the current generated by continuous pressure stimuli. (h) The intelligent textile system simulates the learning-forgetting-relearning behavior of fingertip pressing.

BiOI/TiO$_2$ textile memristor has been fabricated as an artificial synaptic unit, where the Cu@C$_f$ electrode serves as the presynaptic neuron and the C$_f$ electrode serves as the postsynaptic neuron. The physical photos of the intelligent textile system are shown in Fig. S20 in the ESM.

Drawing from the aforementioned favorable RS characteristics, the conductivity of the textile memristor unit was used as synaptic weight, and its increase (or decrease) can be explained as a promotion (or inhibition) process similar to biological synapses. PPF and PPD are well-known features for synaptic devices to reflect short-term plasticity (STP) [23]. The amplitude of the response elicited by the second pulse in a memristor exceeds that of the first pulse when two successive pulses are administered (Fig. 6(c)). This phenomenon is contingent upon the temporal interval separating the two pulses. Figure 6(d) illustrates the typical STP of PPF and PPD characteristics in BiOI/TiO$_2$@C$_f$ textile memristors. When subjected to a pair of pre-synaptic stimuli consisting of pulses with an amplitude and duration of ±1.5 V and 0.02 s, respectively, the PPF index achieves approximately 67.1% at a time interval (Δt) of 0.005 s. However, as the Δt is extended from 0.005 to 1 s, the PPF index diminishes to around 6.7%. The PPF index decays exponentially with increasing time intervals, which is similar to biological systems and corresponds to the memristor's high sensitivity to information processing [12, 23, 47]. By fitting with the following formula

$$\mathrm{PPF} = \frac{G_2 - G_1}{G_1} \times 100\% = C_1 \mathrm{e}^{-\Delta t/\tau_1} + C_2 \mathrm{e}^{-\Delta t/\tau_2} \quad (1)$$

where G_1 and G_2 represent the conductance values following the application of the first and second pulses, respectively, τ_1 and τ_2 denote the time fitting constants, and the derived lines demonstrate a strong correlation with the experimental data. The fitted τ_1 and τ_2 are 8(4) and 612(511) ms for positive (negative) pulses, respectively. In contrast, a smaller (or larger) Δt tends to maintain the device in a state of high (or low) conductance, while an adequately extended Δt does not induce any further alterations in the conductance of the device. These observations align with the principles underlying biological synaptic learning and forgetting.

Repeated learning and training can lead to the transformation of STP to long-term plasticity (LTP), which is manifested as continuous pulse stimulation in memristor studies [44]. To simulate the behavior of biological synapses, Fig. 6(e) examines the phenomena of potentiation and depression in response to a series of 20 continuous, identical voltage pulses, specifically ±1.5 V, each with a duration of 0.02 s and an interval of 0.03 s. The observed current under positive voltage scanning increases from 28.9 μA during the first pulse to 69.3 μA by the twentieth pulse, and the corresponding values under negative voltage are −68.6 to −24.8 μA. The device is set after about 8 positive pulses and can be reset with about 10 negative pulses. The conductivity continuous change device under this pulse stimulation can withstand nearly 200 cycles (Fig. S21 in the ESM). The memristor conductance undergoes significant changes during the initial pulse events of each sequence and subsequently responds to variations in positive and negative pulses, thereby confirming the influence of pulse-driven conduction control on the memristor [23]. In addition, pulse voltages of different amplitudes enable the textile memristor to exhibit clear multivalued storage performance (Fig. 6(f)) [48]. As the forward voltage increases from 1 to 2 V, the conductance of the memristor shows a gradual increase and demonstrates stability in resistance retention. As a negative pulse voltage of −2 V is applied to the device, the conductivity can be restored to its initial state, demonstrating the memristive property of continuously adjustable conductivity.

A high-performance thin-film pressure sensor serves as the initial component of the intelligent textile system. This intelligent textile system calibrates the piezoresistive sensor to capture presynaptic signals, which are subsequently relayed to the memristor for additional storage and classification processes. $BiOI/TiO_2@C_f$ is sensitive to pulse stimuli with a wide range of voltages from 0.2 to 2.5 V (Fig. S22 in the ESM), which is advantageous for selecting the voltage magnitude and sensor parameters to be loaded on the intelligent textile system. Figure S23 in the ESM shows response resistance curve, when the sensor actuated by a force curve tester. The resistance change of the pressure sensor will also cause a change in the voltage applied to the subsequent memristor. Therefore, we selected pressures of 0.5, 1.5, 4, and 10 kPa to be applied to the sensor, in order to simulate the voltage received by the subsequent memristor, which is consistent with that shown in the Fig. 6(f). Applying 80 consecutive stimuli of four types of pressure to the system resulted in a gradual increase in current response, with the number of presses positively correlated with the current value, indicating that the system can remember the pressing actions (Fig. 6(g)). When the applied pressure is 0.5 kPa, the system current response increases from 0.18 to 0.32 μA, which is an order of magnitude difference compared to the increase from 5.43 to 5.66 μA at 1.5 kPa. When the pressure is raised to 10 kPa, the corresponding values are from 16.2 to 19.05 μA. According to actual measurements, when the pressure is 0.5 kPa, the voltage received by the memristor is about 0.49 V, which does not reach the set voltage of the memristor device. Therefore, this order of magnitude difference in conductivity may be due to the fact that the pulse voltage at 0.5 kPa did not form a complete conductive filament. With the increase in the number of pressing stimulation cycles, the learning–forgetting–relearning behavior can be realized in a smart textile system. As shown in Fig. 6(h), during the first learning process (pressure = 1.5 kPa), we used 80 pressing cycles to stimulate the textile memristor. After stopping the pressing for 1 min, the same standard pressing was reapplied to the system for the relearning phase, and it was found that 50 pressing stimuli could achieve the same conductivity level as the first learning process. In the subsequent relearning stage, 20 pressure stimuli were also able to reach the previous conductivity level, indicating that the history of the learning cycle will affect the efficiency of subsequent learning.

A neural network with three layers was constructed to recognize hand gestures such as press, pinch, clamp, and grip. By collecting waveforms of each finger pressing state through sensors, 2000 images were created as the training and testing sets, respectively. This network consists of 550 input neurons, 256 hidden neurons, and 4 output neurons, which recognize and classify the obtained waveforms, thus achieving the recognition of the hand gestures (Fig. 7(a)). Based on the aforementioned research on synaptic functionality, continuous changes in conductivity caused by electrical pluses, superior switching ratio, self-rectifying characteristics, and the NDR effects, the image generated by five fingers pressing is converted into a 110 × 5 pixel version for matrix operation weight update. Figure 7(b) shows the impact of adding different noise datasets (0%, 10%, and 20%) on the performance of neural networks. The hand gestures recognition rate reaches up to 98.5% without adding noisy datasets, the recognition rate is also above 60% after adding a 20% noisy dataset. Moreover, the precision, recall, and specificity values of our textile memristor performance for hand gestures are calculated as a comprehensive analysis (Table S3 in the ESM). The results indicate that the trained network still has good noise tolerance even after receiving different noise test datasets. Figure 7(c) indicates that after 150 training epochs, each gesture's identification accuracy is outstanding, with over 960 correct recognition times across the 4000 test sets. By comparing the calculated results with the labeled test datasets, a confusion matrix of the intelligent textile system classification results was obtained, demonstrating the classification performance of the network [47]. After multiple training cycles, the correct classification percentage corresponding to each gesture is displayed on the diagonal of the confusion matrix. From the training results of the intelligent textile system after 1, 50, and 150 training cycles, it can be seen that the recognition accuracy improves with the increase of training cycles, proving that the system has good recognition and classification capabilities (Fig. 7(d)).

4 Conclusions

In summary, this work constructs an intelligent textile system by weaving carbon fiber with $BiOI/TiO_2$ heterogeneous interface. The obtained textile memristor arrays show an average set voltage of ≈ 0.78 V, high cycling uniformity, and long retention time. The simultaneous occurrence of self-rectification, the room-temperature NDR effect, and biological synaptic behavior, in conjunction with the aforementioned superior performance, is expected to advance the development of flexible information processing systems that are integrated with electronic textiles. Importantly, the designed intelligent textile system simulates memory behavior under different pressure stimuli. Inspired by this, artificial neural network learning methods are applied to human gesture recognition. Under the condition of adding noisy datasets, the recognition rates of gestures reached 98.5% and remained above 60%/80%. The

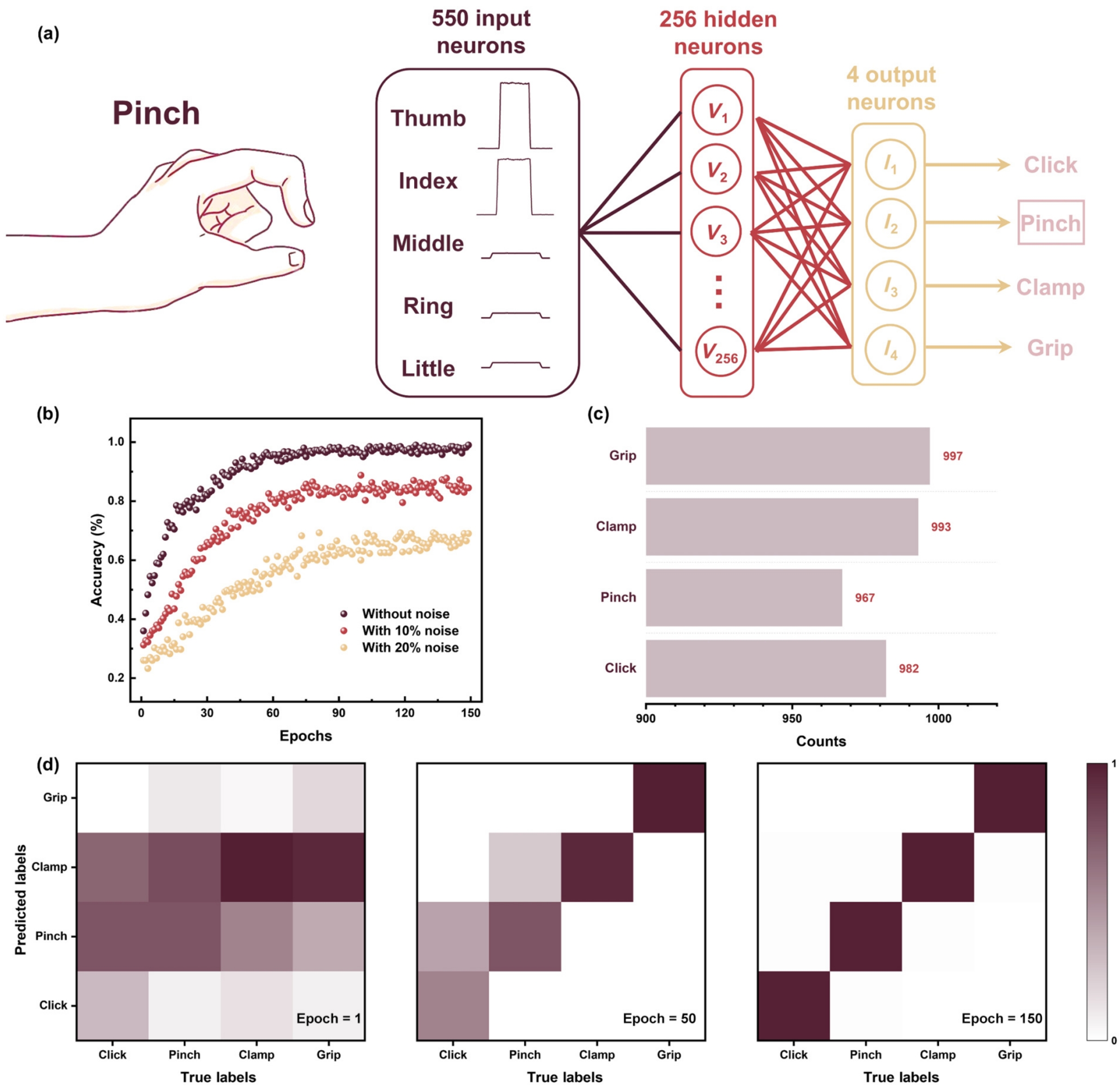

Figure 7 (a) Neural network structure diagram for hand gestures recognition. (b) The recognition rate under different noise ratios (0, 10%, and 20%). (c) The number of correctly recognized hand gestures in the test set after 150 epochs of training. (d) The confusion matrix generated during different cyclic training epoch.

constructed memristor array has the potential to function as a real-time memory system and an integrated recognition tool within computational frameworks, demonstrating a high level of accuracy. With the subsequent addition of display and power supply, there will be exciting use scenarios in the future.

Electronic Supplementary Material: Supplementary material (SEM, EDS mapping, XPS spectra, statistical distribution of memristive performance and mechanical properties of the device, etc.) is available in the online version of this article at https://doi.org/10.26599/NR.2025.94907367.

Data availability

All data needed to support the conclusions in the paper are presented in the manuscript and the Electronic Supplementary Material. Additional data related to this paper may be requested from the corresponding author upon request.

Acknowledgements

This work was supported by the Hunan Science and Technology Innovation Talents Program (No. 2021RC3003).

Declaration of competing interest

All the contributing authors report no conflict of interests in this work.

Author contribution statement

C. J.: Conceptualization, data curation, writing – original draft. S. L. H.: Data curation, validation, writing – original draft. Y. T. Y.: Methodology, software, visualization. Z. X. Z.: Resources, project administration. Y. L. C.: Resources, writing – review & editing, supervision. Y. A. H.: Supervision, writing – review & editing. C. H. Z.: Supervision, writing – review & editing. D. Z.: Conceptualization, supervision, writing – review & editing. Z. Z. D:

Conceptualization, supervision, writing – review & editing. All authors have read and approved the final manuscript.

Use of AI statement

None.

References

[1] Rao, Z. W.; Wang, X. F.; Mao, S. S.; Qin, J. J.; Yang, Y. S.; Liu, M. N.; Ke, C.; Zhao, Y.; Sun, B. Flexible memristor-based nanoelectronic devices for wearable applications: A review. *ACS Appl. Nano Mater.* **2023**, *6*, 18645–18669.

[2] Wang, P. P.; Hu, M. M.; Wang, H.; Chen, Z.; Feng, Y. P.; Wang, J. Q.; Ling, W.; Huang, Y. The evolution of flexible electronics: From nature, beyond nature, and to nature. *Adv. Sci.* **2020**, *7*, 2001116.

[3] Mercante, L. A.; Andre, R. S.; Facure, M. H. M.; Correa, D. S.; Mattoso, L. H. C. Recent progress in conductive electrospun materials for flexible electronics: Energy, sensing, and electromagnetic shielding applications. *Chem. Eng. J.* **2023**, *465*, 142847.

[4] Luo, Y. F.; Abidian, M. R.; Ahn, J. H.; Akinwande, D.; Andrews, A. M.; Antonietti, M.; Bao, Z. N.; Berggren, M.; Berkey, C. A.; Bettinger, C. J. et al. Technology roadmap for flexible sensors. *ACS Nano* **2023**, *17*, 5211–5295.

[5] Liu, S. B.; Cheng, Y.; Han, F.; Fan, S. N.; Zhang, Y. P. Multilevel resistive switching memristor based on silk fibroin/graphene oxide with image reconstruction functionality. *Chem. Eng. J.* **2023**, *471*, 144678.

[6] Rao, M.Y.; Tang, H.; Wu, J. B.; Song, W. H.; Zhang, M.; Yin, W. B.; Zhuo, Y.; Kiani, F.; Chen, B.; Jiang, X. Q. et al. Thousands of conductance levels in memristors integrated on CMOS. *Nature* **2023**, *615*, 823–829.

[7] Teja Nibhanupudi, S. S.; Roy, A.; Veksler, D.; Coupin, M.; Matthews, K. C.; Disiena, M.; Ansh; Singh, J. V.; Gearba-Dolocan, I. R.; Warner, J. et al. Ultra-fast switching memristors based on two-dimensional materials. *Nat. Commun.* **2024**, *15*, 2334.

[8] Zhang, W. B.; Yao, P.; Gao, B.; Liu, Q.; Wu, D.; Zhang, Q. T.; Li, Y. K.; Qin, Q.; Li, J. M.; Zhu, Z. H. et al. Edge learning using a fully integrated neuro-inspired memristor chip. *Science* **2023**, *381*, 1205–1211.

[9] Kim, S. E.; Lee, J. G.; Ling, L. O.; Liu, S. E.; Lim, H. K.; Sangwan, V. K.; Hersam, M. C.; Lee, H. S. Sodium-doped titania self-rectifying memristors for crossbar array neuromorphic architectures. *Adv. Mater.* **2022**, *34*, 2106913.

[10] Hu, S. M.; Yue, J. L.; Jiang, C.; Tang, X. Z.; Huang, X. Z.; Du, Z. J.; Wang, C. Q. Resistive switching behavior and mechanism in flexible $TiO_2@C_f$ memristor crossbars. *Ceram. Int.* **2019**, *45*, 10182–10186.

[11] Yadav, R.; Poudyal, S.; Rajarapu, R.; Biswal, B.; Barman, P. K.; Kasiviswanathan, S.; Novoselov, K. S.; Misra, A. Low power volatile and nonvolatile memristive devices from 1D MoO_2-MoS_2 core–shell heterostructures for future bio-inspired computing. *Small* **2023**, *20*, 2309163.

[12] Lei, P. X.; Duan, H.; Qin, L.; Wei, X. H.; Tao, R.; Wang, Z. G.; Guo, F.; Song, M. L.; Jie, W. J.; Hao, J. H. High-performance memristor based on 2D layered BiOI nanosheet for low-power artificial optoelectronic synapses. *Adv. Funct. Mater.* **2022**, *32*, 2201276.

[13] Wang, T. Y.; Meng, J. L.; Zhou, X. F.; Liu, Y.; He, Z. Y.; Han, Q.; Li, Q. X.; Yu, J. J.; Li, Z. H.; Liu, Y. K. et al. Reconfigurable neuromorphic memristor network for ultralow-power smart textile electronics. *Nat. Commun.* **2022**, *13*, 7432.

[14] Liu, Y.; Zhou, X. F.; Yan, H.; Shi, X.; Chen, K.; Zhou, J. Y.; Meng, J. L.; Wang, T. Y.; Ai, Y. L.; Wu, J. X. et al. Highly reliable textile-type memristor by designing aligned nanochannels. *Adv. Mater.* **2023**, *35*, 2301321.

[15] Liu, Y.; Zhou, X. F.; Yan, H.; Zhu, Z. F.; Shi, X.; Peng, Y. H.; Chen, L.; Chen, P. N.; Peng, H. S. Robust memristive fiber for woven textile memristor. *Adv. Funct. Mater.* **2022**, *32*, 2201510.

[16] Lee, M. J.; Kim, S. I.; Lee, C. B.; Yin, H. X.; Ahn, S. E.; Kang, B. S.; Kim, K. H.; Park, J. C.; Kim, C. J.; Song, I. et al. Low-temperature-grown transition metal oxide based storage materials and oxide transistors for high-density non-volatile memory. *Adv. Funct. Mater.* **2009**, *19*, 1587–1593.

[17] Mao, S. S.; Sun, B.; Ke, C.; Qin, J. J.; Yang, Y. S.; Guo, T.; Wu, Y. A.; Shao, J. Y.; Zhao, Y. Evolution between CRS and NRS behaviors in $MnO_2@TiO_2$ nanocomposite based memristor for multi-factors-regulated memory applications. *Nano Energy* **2023**, *107*, 108117.

[18] Ismail, M.; Chand, U.; Mahata, C.; Nebhen, J.; Kim, S. Demonstration of synaptic and resistive switching characteristics in $W/TiO_2/HfO_2/TaN$ memristor crossbar array for bioinspired neuromorphic computing. *J. Mater. Sci. Technol.* **2022**, *96*, 94–102.

[19] Wan, F. X.; Wang, Q. W.; Harumoto, T.; Gao, T. H.; Ando, K.; Nakamura, Y.; Shi, J. Truly electroforming-free memristor based on TiO_2–CoO phase-separated oxides with extremely high uniformity and low power consumption. *Adv. Funct. Mater.* **2020**, *30*, 2007101.

[20] Lu, C.; Meng, J. L.; Song, J. R.; Wang, T. Y.; Zhu, H.; Sun, Q. Q.; Zhang, D. W.; Chen, L. Self-rectifying all-optical modulated optoelectronic multistates memristor crossbar array for neuromorphic computing. *Nano Lett.* **2024**, *24*, 1667–1672.

[21] Kim, T. H.; Lee, J.; Kim, S.; Park, J.; Park, B. G.; Kim, H. 3-bit multilevel operation with accurate programming scheme in TiO_x/Al_2O_3 memristor crossbar array for quantized neuromorphic system. *Nanotechnology* **2021**, *32*, 295201.

[22] Wang, Z. R.; Joshi, S.; Savel'ev, S. E.; Jiang, H.; Midya, R.; Lin, P.; Hu, M.; Ge, N.; Strachan, J. P.; Li, Z. Y. et al. Memristors with diffusive dynamics as synaptic emulators for neuromorphic computing. *Nat. Mater.* **2017**, *16*, 101–108.

[23] Wei, W. B.; Sun, H.; Dong, X. F.; Lu, Q.; Yang, F. X.; Zhao, Y.; Chen, J. T.; Zhang, X. Q.; Li, Y. A neotype self-rectifying Cu_3SnS_4-MoO_3 synaptic memristor for neuromorphic applications. *Chem. Eng. J.* **2024**, *482*, 148848.

[24] Zhang, Y.; Sun, A. R.; Xiong, M. Y.; Macharia, D. K.; Liu, J. S.; Chen, Z. G.; Li, M.; Zhang, L. S. TiO_2/BiOI p-n junction-decorated carbon fibers as weavable photocatalyst with UV-vis photoresponsive for efficiently degrading various pollutants. *Chem. Eng. J.* **2021**, *415*, 129019.

[25] Li, Q. B.; Qin, H.; Zhao, H. K.; Zhao, X.; Cheng, X F..; Fan, W. L. Facile fabrication of a BiOI/TiO_2 p–n junction via a surface charge-induced electrostatic self-assembly method. *Appl. Surf. Sci.* **2018**, *457*, 59–68.

[26] Li, Z. R.; Wang, J. B.; Tong, Y. J.; Xiao, S. J.; Xu, L. H. Microstructural evolution during oxidative ablation in air for polyacrylonitrile based carbon fibers with different graphite degrees. *Surf. Interface Anal.* **2013**, *45*, 787–792.

[27] Yao, S. Y.; Li, Y. X.; Zhao, C. Z.; Wang, F. Y.; Bai, Y. J.; Wang, Y.; Zhu, Z. T.; Chen, H. Optimization of the cycle numbers of TiO_2 resistive random-access memory devices by annealing. *ACS Appl. Electron. Mater.* **2023**, *5*, 1196–1205.

[28] Balachandran, U.; Eror, N. G. Raman spectra of titanium dioxide. *J. Solid State Chem.* **1982**, *42*, 276–282.

[29] Zhang, B. K.; Wang, D. B.; Jiao, S. J.; Xu, Z. K.; Liu, Y. X.; Zhao, C. C.; Pan, J. W.; Liu, D. H.; Liu, G.; Jiang, B. J. et al. TiO_{2-x} mesoporous nanospheres/BiOI nanosheets S-scheme heterostructure for high efficiency, stable and unbiased photocatalytic hydrogen production. *Chem. Eng. J.* **2022**, *446*, 137138.

[30] Yang, H. H.; Hsiao, K. Y.; Liu, F. Y.; Chen, C. C.; Chen, I. C. Vibrational structures of iodine-vacancy bismuth oxyiodides using temperature-dependent low-wavenumber raman spectroscopy. *J. Phys. Chem. C* **2024**, *128*, 563–570.

[31] Seok, J. Y.; Song, S. J.; Yoon, J. H.; Yoon, K. J.; Park, T. H.; Kwon, D. E.; Lim, H.; Kim, G. H.; Jeong, D. S.; Hwang, C. S. A review of three-dimensional resistive switching cross-bar array memories from the integration and materials property points of view. *Adv. Funct. Mater.* **2014**, *24*, 5316–5339.
[32] Jang, Y. H.; Han, J.; Kim, J.; Kim, W.; Woo, K. S.; Kim, J.; Hwang, C. S. Graph analysis with multifunctional self-rectifying memristive crossbar array. *Adv. Mater.* **2023**, *35*, 2209503.
[33] Pant, R.; Patel, N.; Nanda, K. K.; Krupanidhi, S. B. Negative differential resistance and resistive switching in SnO_2/ZnO interface. *J. Appl. Phys.* **2017**, *122*, 125303.
[34] Herzig, M.; Weiher, M.; Ascoli, A.; Tetzlaff, R.; Mikolajick, T.; Slesazeck, S. Multiple slopes in the negative differential resistance region of NbO_x-based threshold switches. *J. Phys. D: Appl. Phys.* **2019**, *52*, 325104.
[35] Weiher, M.; Herzig, M.; Tetzlaff, R.; Ascoli, A.; Mikolajick, T.; Slesazeck, S. Pattern formation with locally active S-type NbO_x memristors. *IEEE Trans. Circuits Syst. I: Regul. Pap.* **2019**, *66*, 2627–2638.
[36] Yang, C.; Wang, H. Y.; Zhou, G. D.; Qin, S. D.; Hou, W. T.; Zhu, S. H.; Zhao, Y.; Sun, B. A multifunctional memristor with coexistence of NDR and RS behaviors for logic operation and somatosensory temperature sensing applications. *Nano Today* **2024**, *57*, 102382.
[37] Wang, H. T.; Li, C. L.; Banerjee, S.; He, S. B. Novel memristor and memristor-based applications. *Eur. Phys. J. Spec. Top.* **2022**, *231*, 2973–2977.
[38] Yang, L.; Chen, Y.; Xu, Z. Z.; Xia, H.; Natuski, T.; Xi, Y. S.; Ni, Q. Q. Effect of surface modification of carbon fiber based on magnetron sputtering technology on tensile properties. *Carbon* **2023**, *204*, 377–386.
[39] Prada, S.; Rosa, M.; Giordano, L.; Di Valentin, C.; Pacchioni, G. Density functional theory study of TiO_2/Ag interfaces and their role in memristor devices. *Phys. Rev. B* **2011**, *83*, 245314.
[40] Xu, H.; Akbari, M. K.; Verpoort, F.; Zhuiykov, S. Nano-engineering and functionalization of hybrid Au-Me_xO_y-TiO_2 (Me = W, Ga) hetero-interfaces for optoelectronic receptors and nociceptors. *Nanoscale* **2020**, *12*, 20177–20188.
[41] Lampert, M. A.; Schilling, R. B. Current injection in solids: The regional approximation method. *Semicond. Semimetals* **1970**, *6*, 1–96.
[42] Ling, S. T.; Lin, S. R.; Wu, Y. Z.; Li, Y. Toward highly-robust MXene hybrid memristor by synergetic ionotronic modification and two-dimensional heterojunction. *Chem. Eng. J.* **2024**, *486*, 150100.
[43] Zhang, L.; Yu, H.; Xiao, C. C.; Si, J. W.; Xu, H. Y.; Zhu, W. H.; Wang, L. C. Building light stimulated synaptic memory devices for visual memory simulation. *Adv. Electron. Mater.* **2021**, *7*, 2000945.
[44] Pan, F.; Chen, C. *Resistive Random Access Memory Materials and Devices*; China Science Publishing, 2014.
[45] Wang, Z.; Griffin, P. B.; McVittie, J.; Wong, S.; McIntyre, P. C.; Nishi, Y. Resistive switching mechanism in $Zn_xCd_{1-x}S$ nonvolatile memory devices. *IEEE Electron Device Lett.* **2007**, *28*, 14–16.
[46] Yang, Y. C.; Pan, F.; Liu, Q.; Liu, M.; Zeng, F. Fully room-temperature-fabricated nonvolatile resistive memory for ultrafast and high-density memory application. *Nano Lett.* **2009**, *9*, 1636–1643.
[47] Wang, Y. L.; Su, J.; Ouyang, G. Y.; Geng, S. Y. Y.; Ren, M. C.; Pan, W. L.; Bian, J.; Cao, M. H. Flexible Zn-TCPP nanosheet-based memristor for ultralow-power biomimetic sensing system and high-precision gesture recognition. *Adv. Funct. Mater.* **2024**, *34*, 2316397.
[48] Pei, Y. F.; Li, Z. Q.; Li, B.; Zhao, Y.; He, H.; Yan, L.; Li, X. Y.; Wang, J. J.; Zhao, Z.; Sun, Y. et al. A multifunctional and efficient artificial visual perception nervous system with Sb_2Se_3/CdS-Core/Shell (SC) nanorod arrays optoelectronic memristor. *Adv. Funct. Mater.* **2022**, *32*, 2203454.